

Electronic Removal of Encrustations Inside the Steinheim Cranium Reveals Paranasal Sinus Features and Deformations, and Provides a Revised Endocranial Volume Estimate

HERMANN PROSSINGER,* HORST SEIDLER, LOTHAR WICKE, DAVE WEAVER, WOLFGANG RECHEIS, CHRIS STRINGER, AND GERD B. MÜLLER

Features in the endocranium, as revealed by computed tomography (CT) scans of largely complete mid-Pleistocene crania, have helped elucidate unexpected affinities in the genus *Homo*. Because of its extensive encrustations and deformations, it has been difficult to repeat such analyses with the Steinheim cranium. Here, we present several advances in the analysis of this *Homo heidelbergensis* cranium by applying filter algorithms and image editing techniques to its CT scan. First, we show how the encrustations have been removed electronically, revealing interesting peculiarities, particularly the many directions of the deformations. Second, we point out similarities and differences between the frontal and sphenoidal sinuses of the Steinheim, Petralona, and Broken Hill (Kabwe) crania. Third, we assess the extent of the endocranial deformations and, fourth, their implications for our estimation of the braincase volume. *Anat Rec (Part B: New Anat)* 273B:132–142, 2003. © 2003 Wiley-Liss, Inc.

KEY WORDS: Steinheim; computed tomography; CT; imaging; fossil; encrustation; endocranial volume; endocast; *Homo heidelbergensis*

INTRODUCTION

The Steinheim cranium was found in a gravel pit near Steinheim, Germany, by Karl Sigris in 1933 (Berckheimer, 1933; Weinert, 1936) and is tentatively dated around 250,000 years BP (Weinert, 1936; Adam, 1985). Because it is

strongly deformed and extensively filled with “mineralized” sediments, discussion of its morphologic similarity and potential taxonomic affinity with other late mid-Pleistocene crania has, heretofore, been hampered. This same difficulty is encountered in

many other fossil crania. The electronic methods of removing such sedimentations we present here, thus, expands the paleoanthropologists’ toolkit, because, as we show in this article, descriptions of skulls with sedimentation removed may contribute to a re-

Dr. Prossinger is Adjunct Associate Professor of Biomathematics at the Institute of Anthropology, University of Vienna. In addition to developing segmentation algorithms, he models growth phenomena of populations and fractal growth processes in physiological systems. Dr. Seidler is Full Professor at the same institute. He supervises many research projects, involving mummies in the Peruvian Andes, archaic *Homo* teeth in Novosibirsk, Russia, as well as human evolution studies. Dr. Wicke is a radiologist at the Institute for Diagnostic Imaging, Rudolfinerhaus Hospital, Vienna, and Adjunct Associate Professor at the same institute. He has studied the Petralona skull CT scan extensively. Dr. Weaver is Professor emeritus at the Department of Anthropology, Wake Forest University, Winston-Salem, NC. His major specialty is the study of bone physiology and histology. Dr. Recheis is a physicist working in the Department of Radiology II, University Hospital, Innsbruck, Austria,

where he develops techniques to optimally scan fossil specimens and produce stereolithographs of them. Dr. Stringer is in the Human Evolution Unit, Museum of Natural History, London. He specializes in the macromorphology of *Homo* crania, especially early *H. sapiens* and *H. Neanderthalensis*. Dr. Müller is Professor at the Department of Zoology, University of Vienna, and Research Director, Konrad Lorenz Institute for Evolution and Cognition Research, Altenberg, Austria. His research topics include evolution-development issues and cognitive evolution of the human brain.

*Correspondence to: Hermann Prossinger, Institute for Anthropology, University of Vienna, Althanstrasse 14, A-1090 Vienna. Fax: +43-1-4277-9547; E-mail: hermann.prossinger@univie.ac.at

DOI 10.1002/ar.b.10022
Published online in Wiley InterScience (www.interscience.wiley.com).

**Descriptions of skulls
with sedimentation
removed may
contribute to a revision
of assessing
morphologic features.**

vision of assessing morphologic features. Such revisions will perhaps clarify contentious issues about the skulls’ place in putative evolutionary trees.

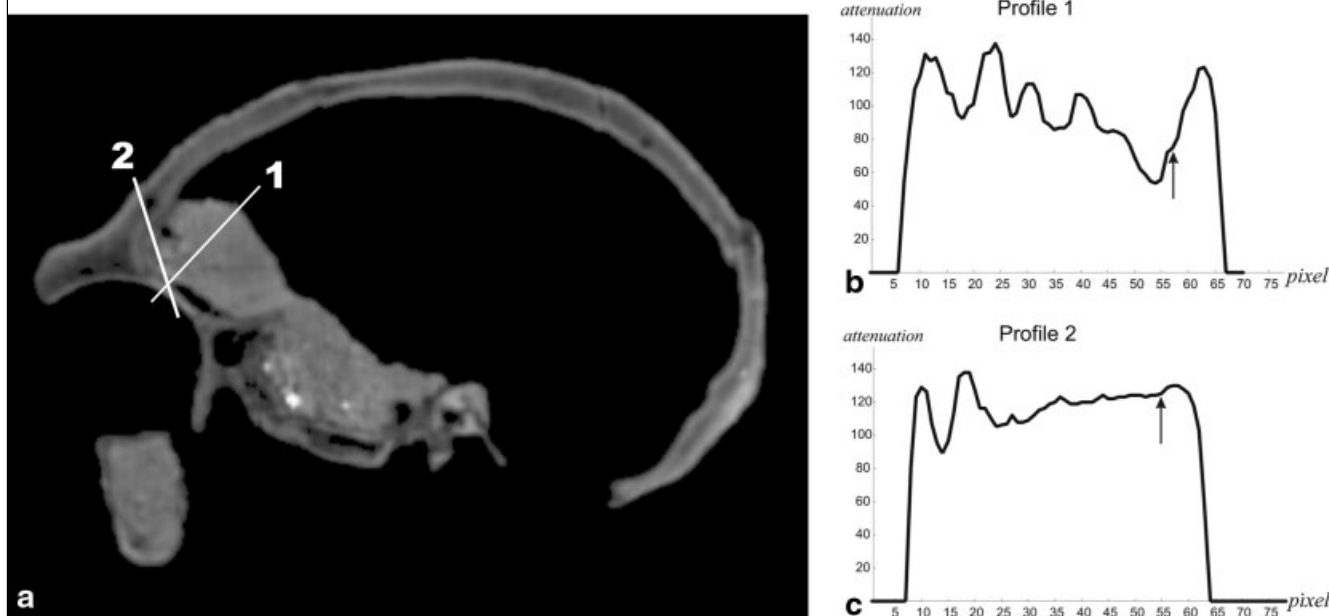
Fossilized skulls rarely (if ever) fossilize in isolation; they are embedded

Box 1. Variation of X-Ray Attenuation in Fossilized Samples

Analysis of two “lines” (Box 1, Figure a) across one slice of a CT scan of the Steinheim cranium shows how attenuation varies along them. There is a slight ‘dip’ (a local minimum) where the putative boundary between fossilized bone and encrustation is to be expected (Box 1, Figure b and c, arrows). Because of three effects, i.e., (1) the narrowness of the gap, (2) the partial volume effect, and (3) the (almost) equal attenuation by the fossil-

ized bone and the encrustation, the actual boundary need not be at the position of the three-dimensional picture region, or voxel, where the dip occurs (See Box 2). Moreover, the “dip voxel” will not have the same attenuation (Hounsfield number) at other points of the putative boundary. Indeed, the minimum value in the boundary voxel may even be higher than the attenuation within some other region of the fossilized

bone or the encrustation—even in the same slice. In an adjacent slice, the Hounsfield numbers may (and usually do) vary in a different way. To summarize: an algorithm that identifies least-valued voxels is not adequately reliable to find the voxels of the sought-after boundary. Note that the attenuation fluctuates more strongly in the encrustation than in the fossilized bone (Box 1, Figure b).



Box 1 Figure. A parasagittal slice of the CT-scan of the Steinheim cranium with encrustation. More precisely, this is a slice of the reorientated and rescaled CT scan. (The scan is orientated so that the Frankfort horizontal is in the x-y plane, and the voxel dimensions have been rescaled to be equal in all three coordinate directions.) **a:** Two lines along which the attenuation profile has been sampled. The putative gap is very close to where the two lines intersect. **b:** The attenuation profile of line 1. **c:** The attenuation profile of line 2. Arrows in the profiles show the “dip,” which in each profile corresponds to the putative gap between fossilized bone and encrustation.

in a matrix of sediments that fossilizes together with them (occasionally the sediment fossilizes after the bone material has already done so). In both cases, the sediment and the fossilized bone have remarkably similar mineral constituents and thus similar attenuations in an x-ray beam during computed tomography (CT) analysis (see Box 1). Only when the linear x-ray absorption coefficient of the sediment is sufficiently different from that of the fossilized specimen can simple thresholding (eliminating the CT sig-

nals above or below a predefined value) in image and/or data analysis be considered adequate to virtually remove it from the CT scan data file. In the case of Steinheim and some other fossil crania, this method will not work. In many regions of the endocranial vault, the sediment appears fused to the fossilized inner table of the frontal vault, because the Hounsfield numbers change insufficiently at the boundary (see Box 1). Hence, many edge-detection algorithms used in medical imaging software cannot be

applied directly and a different methodology must be developed.

SEGMENTATION METHODOLOGY

We have devised an approach—which we call *segmentation methodology*—that can “virtually” or electronically separate fossilized bone from the sedimentation matrix (the “encrustation”; Prossinger et al., 1998). First, we apply a gradient filter to the whole CT scan M (i.e., the data file; a slice is shown in Figure 1a) by comparing the

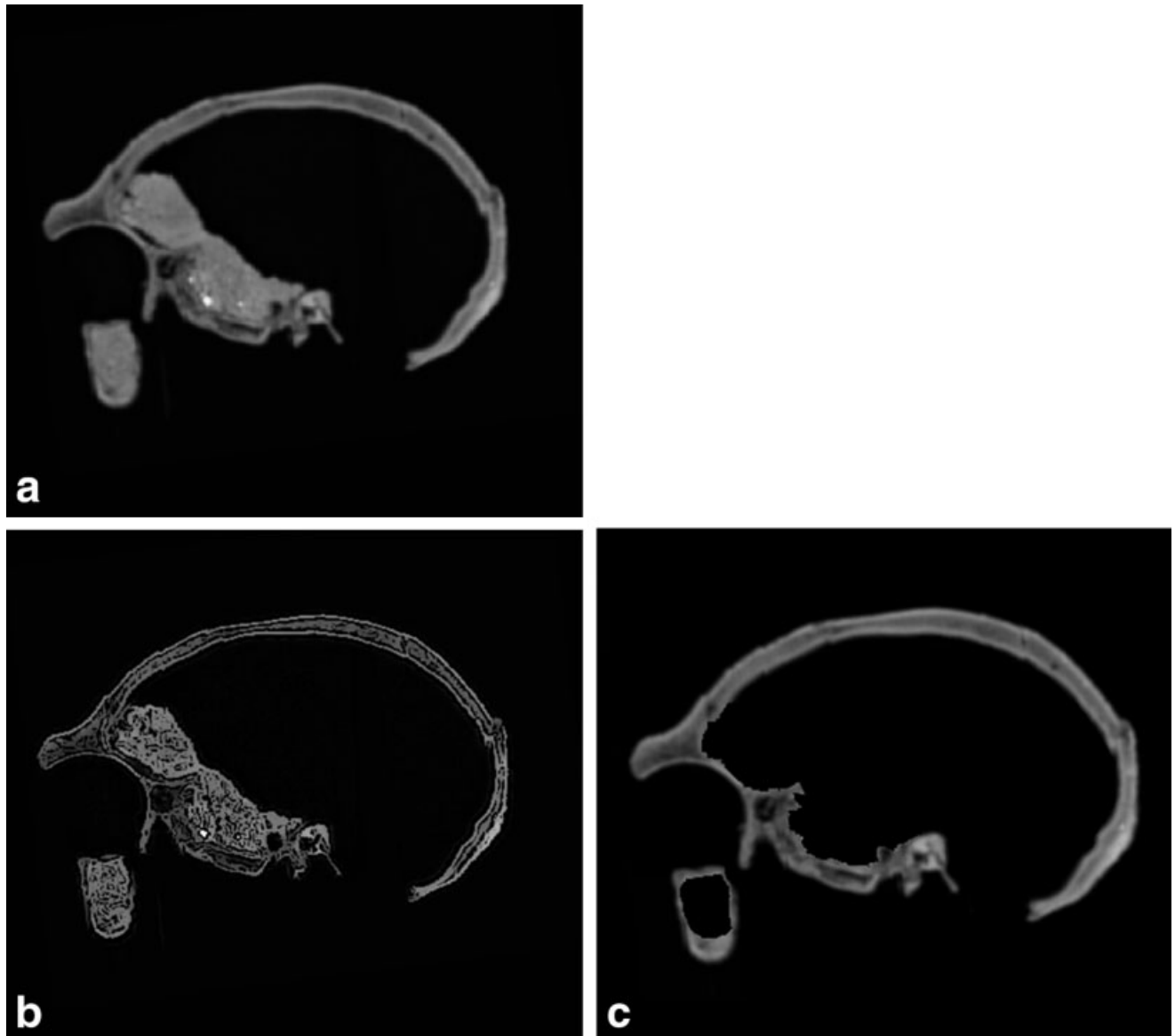


Figure 1. The sequence of steps that lead to a segmentation of the fossil cranium from its encrustations. **a:** A slice together with the encrustations. The white extended dots are attenuation images of pebbles. **b:** The resulting slice image after the sequence of filter steps have been applied. Note that the filter algorithm also finds a boundary between the largest pebble and the rest of the encrustation. **c:** The result after the image-editing removal of those pixels/voxels that were identified by the filter algorithm to be encrustation (see Boxes 1 and 2). Note that the *os petrosum* is very dense (thus, as a fossil it has strong attenuation and large Hounsfield numbers). Manual image editing is necessary to prevent a generalized algorithm from removing it along with the encrustations (which have similar attenuations). The filter algorithm introduces a “jaggedness” (which can be seen in the *tabula interna* of the frontal bone). This “jaggedness” must be removed by a sequence of dilate/erode steps (explained in Box 3), rather than some polynomial interpolation algorithm, which does not (and cannot) consider the underlying anatomical features.

attenuation d (i.e., the Hounsfield number) at each voxel position with the attenuation values in a surrounding cube of length $l = (1 + 2h)$ (see Box 2). This attenuation is replaced by the largest difference g (“steepest descent” or maximum gradient) within the $(l^3 - 1)$ neighboring voxels. The resulting gradient file G of all gradients g barely shows edges where sediment and specimen meet (showing zero

where the putative boundary should be in the fused case). However, because the fossilized compact bone has a relatively smooth variation in d , whereas the sediment exhibits graininess, the values g in G should fluctuate considerably in sediment regions, while being close to zero in the fossilized compact bone, where the attenuation does not vary strongly (Box 1, Figure b,c). Consequently, we applied

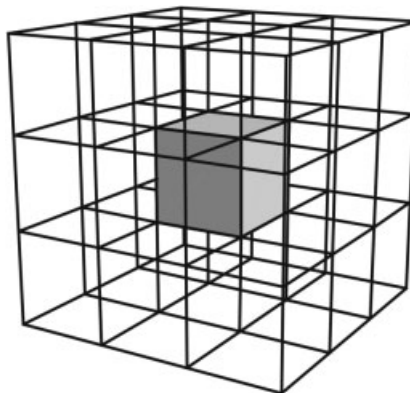
an “unmask” filter (the difference between g and the average within the cube l^3) to G . The linear combination of gradient and unmask filter yielded a useful filtered file F (Figure 1b). We applied standard image editing functions to the regions that now clearly represented the sediment in the filtered file F . We then convoluted this edited filter file F with M to obtain a preliminary result C ; the difference

Box 2. CT Scans of Fossilized Specimens and Boundary Determination

A CT scan is an image file that is the result of x-ray scanning a specimen (in this article, a fossilized bone together with its fossilized sediments). A planar array of x-ray beams is transmitted diametrically through the specimen and detectors on the opposite side measure the attenuation of these beams by the specimen. The array is rotated in the plane; therefore, one obtains the attenuation as a function of angle. From this function, the attenuation at each point (more precisely, in each picture region, or pixel) can be mathematically reconstructed (See Box 1; Hounsfield, 1973). The specimen is then moved along the axis of rotation by a fixed amount (called "slice thickness," which, in medical scanners, is usually between 1.0 and 2.0 mm) and the rotation of the beam arrays, etc., is repeated.

A voxel is the three-dimensional analogue to a pixel: it is a volume element with a pixel as base and the slice thickness as height. The attenuation values stored in each voxel of a CT scan are a measure of the attenuation within that voxel. Typically, the attenuation values (Hounsfield numbers) are scaled from 0 to 4,095 (12-bit scale), with the maximum corresponding to the strongest attenuation and rendered as white on the imaging device.

The transition surface (boundary) between a strongly attenuating region (a fossilized bone, say) and a weakly attenuating region (air, say) often passes through one voxel. The Hounsfield number of this voxel, thus, will be the weighted average of the relative proportions of the two Hounsfield numbers of the adjacent attenuating material. As a conse-



Box 2 Figure. A (cubic) voxel and adjacent voxels. All algorithmic operations discussed in the text relate to these surrounding voxels. In the case of a smoothing algorithm, the attenuation value of a voxel is replaced by the average of the attenuation values of this voxel and its surrounding voxels. The averaging depends on how many surrounding voxels are considered (in this case, $(P-1) = 26$; thus, because $l = (1 + 2h)$, $h = 1$). In the case of "erode" and "dilate" algorithms, one selects which of the surrounding voxels are to be included (for details, see Box 3).

quence, the Hounsfield numbers of voxels along boundaries are some value between those that characterize the attenuation of the strongly and weakly absorbing regions. Despite the many advantages of digitizing images, this partial volume effect is one bane of the digital approach to analysis of three-dimensional objects.

If a gap between two strongly attenuating regions is less than one voxel wide, then, because of the partial volume effect, the Hounsfield number hardly decreases when crossing the gap from one strongly attenuating region to the next. The two regions then appear fused. In the situations studied in this work, fossilized bone and encrustations have almost equal attenuations. The Hounsfield number, therefore, hardly "dips" at the boundary between the two (See Box 1, Figure c), as there rarely is a gap between fossilized bone

and encrustation. There is, therefore, the problem that no algorithm can automatically detect the boundary anthropologists are so keen on finding.

A compounding difficulty (for conventional image-analysis software) is the observation that the attenuation along the strongly attenuating regions is not constant. Yet this difficulty is what we use to our advantage: the fluctuation of the attenuation is much less in fossilized bone than it is in sediments. The trick, therefore, is to subtract a smoothing algorithm output (explained in the caption of Box 2 Figure) from the gradient of the original CT scan. The difference will be considerably larger in the sediment than in the fossilized bone region and the transition between the two in the output file characterizes the boundary (see also Figure 1b in the text).

between M and C is the (raw) sediment file S (Figure 1c). We denote this sediment file "raw", because further manipulations of its surface are necessary (see below).

This sequence of operations ($M \rightarrow G \rightarrow F \rightarrow C \rightarrow S = M - C$) yielded a result that appeared to be anatomically satisfactory (Figure 1c). How-

ever, because all filter operations "probe" the surroundings of an investigated voxel out to a distance h in all three directions, the resulting contour in C (which should be the surface of the fossilized bone) has some "jaggedness" (Figure 1c). Furthermore, there are irregularities and breaks in the fossilized specimen, which will then

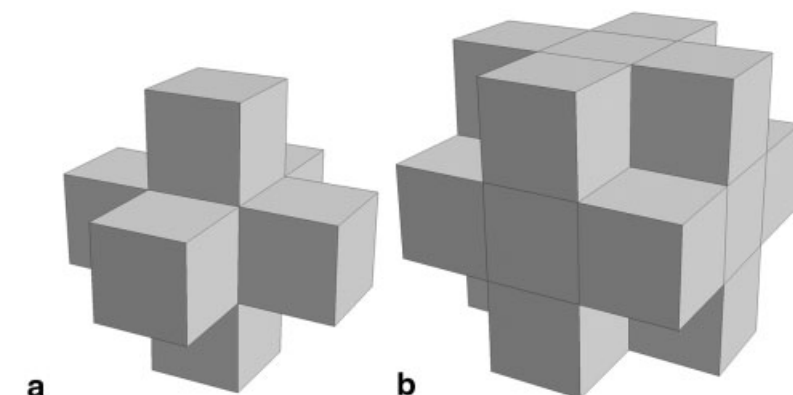
also be partially removed by the process we used to extract the attenuation graininess in M .

We eliminate such artifacts in the preliminary result C by a "smoothing" methodology, which is different from the various conventional interpolation algorithms (such as polynomial splines). To detect the surface to the

Box 3. Erosion and Dilation: Smoothing and Elimination of Artifacts

The erosion of a voxel takes place (i.e., its Hounsfield number is set to 0) if all the voxels surrounding this (central) voxel, as defined by these two structural elements (or even simpler ones, such as a surrounding cube with a connectivity 26, as in Box 2, Figure b), are of the same bit value (namely 0). In the case of *dilation*, voxels at the central position are set to nonzero under the same algorithmic conditions.

These two operations are noncommutative: once a hole, say, has been "filled" by a dilate operation, the masks used for erode will no longer detect its former presence. The erode operation will, in general, remove a layer from the nonzero surface in a CT scan but can no longer open the hole that had been filled. However, if a hole is large enough, then the dilate operation will not completely close it, so it will be restored to its former size after the erode operations (albeit with perhaps differently shaped edges). If a hole is



Box 3 Figure. Two of the types of masks (structuring elements) used for dilate and erode operations. **a:** An object with a connectivity of 6 (a "jack"). **b:** An object with a connectivity of 18 (a "truncated" cube).

large and should still be closed, then several dilate operations are needed before the same number of erode operations are applied to restore the original surface without the hole.

The variation in the types of masks used for each dilate or erode step influences the resulting surface. By

judiciously choosing appropriate masks in a suitable sequence, one can (for example) smooth sharp tips, which are the artifacts of the filtering algorithm, whereas suitably different sets of masks can enhance ridges (usually by including a "jack," as shown in Box 3, Figure a).

nearest voxel, we applied a series of "dilate" and "erode" algorithms to *C* (see Box 3). There are numerous erode/dilate masks of different shapes ("jacks" and "truncated" cubes with different connectivity), and we had to explore the combination that yielded the best results. Cracks and slits in *C* first needed to be filled with dilate operations. As dilation operations also adds layer(s) to smooth surfaces, we eroded off the layers (the erode operation will not open small cracks closed by a dilation because erode/dilate is a noncommutative algorithm combination). To avoid adding spurious features to our edited result *R*, we also eroded/dilated *S*, the sediment file. Any crack filled by a dilate operation in *C* must be matched by the erosion of the ridge in *S*. The difference of the complementary operations on *C* and *S* is a measure of how well the chosen smoothing operations worked.

It would be useful to know to what extent the revealed surface could possibly deviate from the surface at the time of the individual's death. The answer is a numerical reliability/uncer-

tainty estimate (as there exists no possibility of comparison). During the implementations of the erode/dilate steps, we retain all intermediate results; the difference between the outcome and input file *M* allows us to determine the change at each step. We do not reject a procedure step that produces a change by more than one voxel layer, but we do check that the result of several steps does not drift by more than one layer. After all the smoothing operations were implemented, the difference with *M* was one surface voxel over parts of the intact skull surface, most often none at all. Some small regions displayed a difference of two voxel layers, which we suspect to be due to large irregularities there. These may themselves be artifacts, introduced in the original CT scan by trying to suppress surface transition voxels because of the partial volume effect (Spoor et al., 1993, 2000). As most of these two-voxel regions represented anatomically identifiable ridges or sharp edges, we image-edited these manually.

If the described method introduces

no systematic error due to the algorithms used (and inspection indicates that it does not wherever the anatomy can be visually assessed), then the resultant file *R* is a voxel data set representing the CT scan of the Steinheim fossil as if it were without encrustations (Prossinger, 1999; Figure 2b,d).

MORPHOLOGY AND DEFORMATIONS

When one carefully examines the Steinheim fossil and its encrustations, several features are apparent. The external surface of the encrustation in the nasal cavity is not original; it must have been sculpted into its present appearance by one of the preparators (Berkheimer (1933) suspected Böck) long before scanning. The orbit was likewise sculpted, and small sections of the orbital walls appear to have been chipped away in the process (Figure 2b).

By using our imaging technique, we have succeeded in isolating part of the *crista galli* (Figure 3a), several laminae

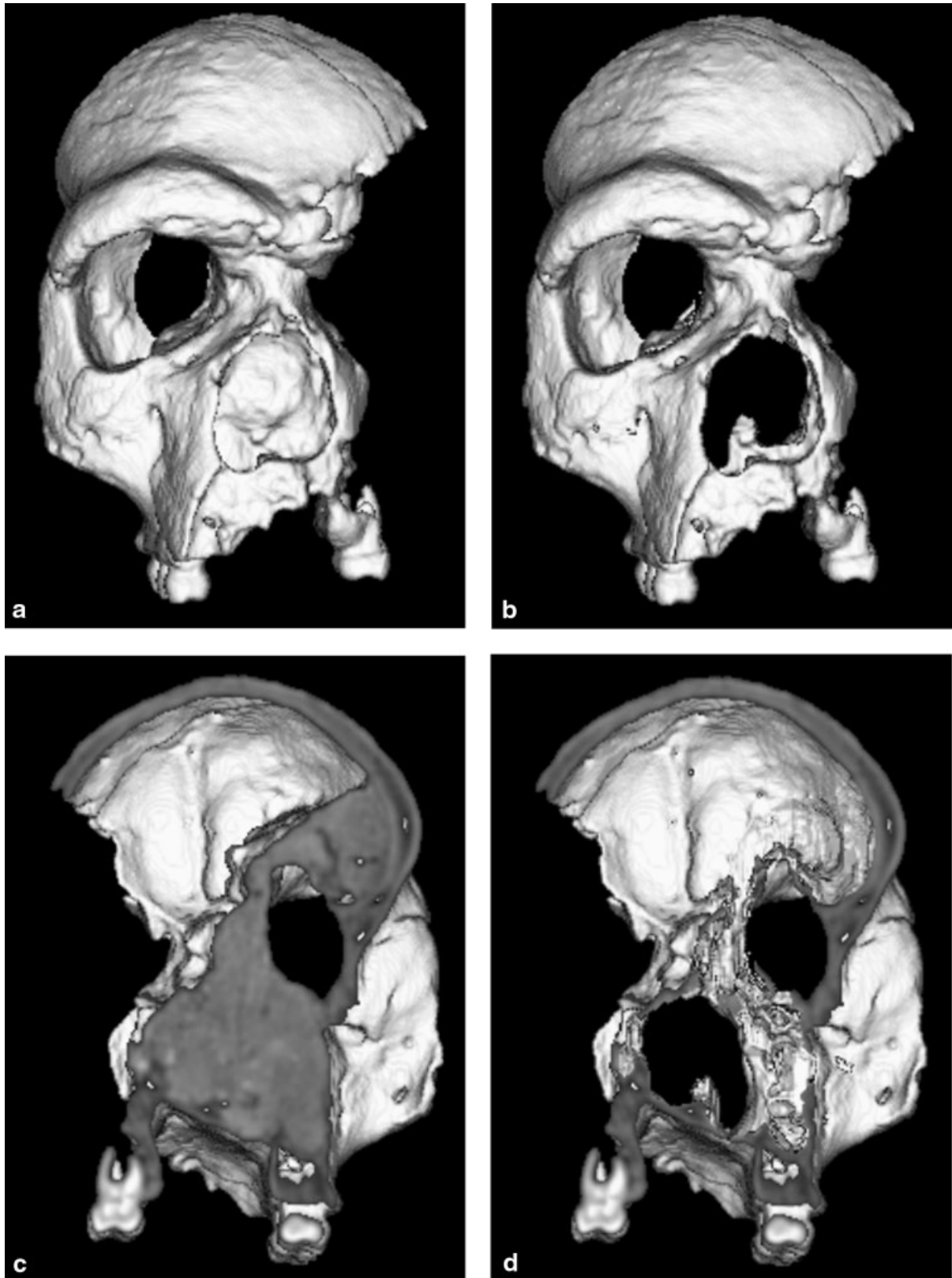


Figure 2. Views of the posterior part of the Steinheim cranium before and after the removal of the sedimentation. **a:** Frontal view with the encrustations. **b:** Frontal view after the removal of the encrustations and applying erode/dilate algorithmic smoothing. **c:** The internal view of the cranium with the encrustations. **d:** The internal view after the removal of the encrustations and applying erode/dilate algorithmic smoothing. In both views, the success of the smoothing algorithm is to be noted: in a, the fossa canina appears smooth; in b, the encrustations inside these foramina have been removed (and the erode/dilate operations have produced reasonably smooth edges of these foramina).

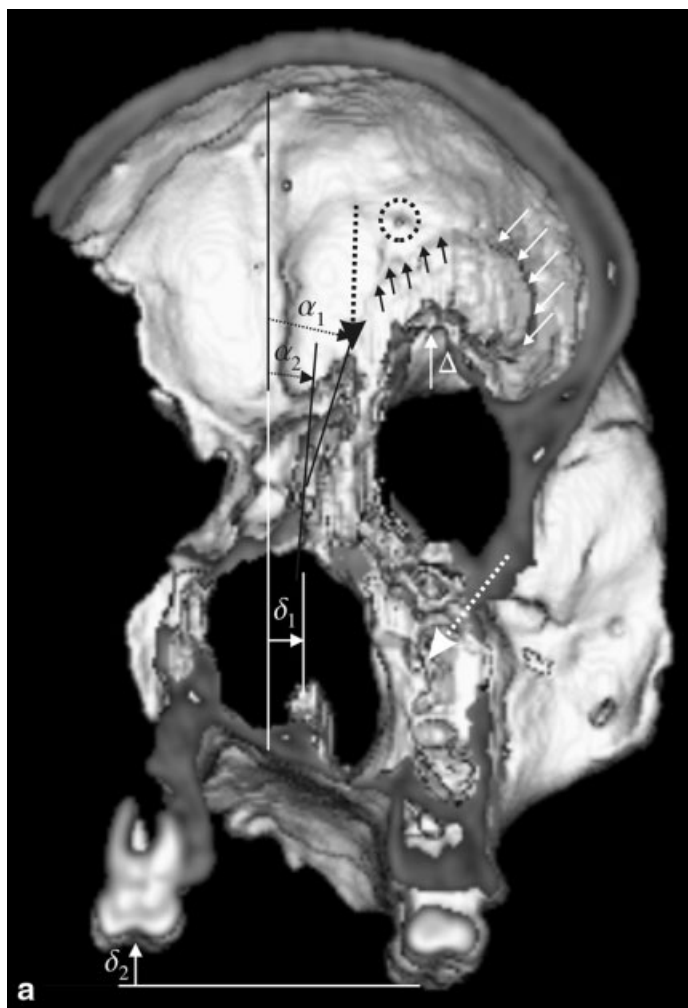
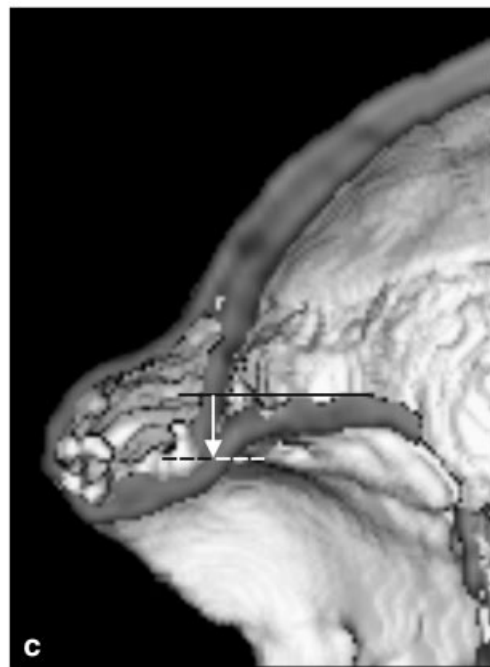
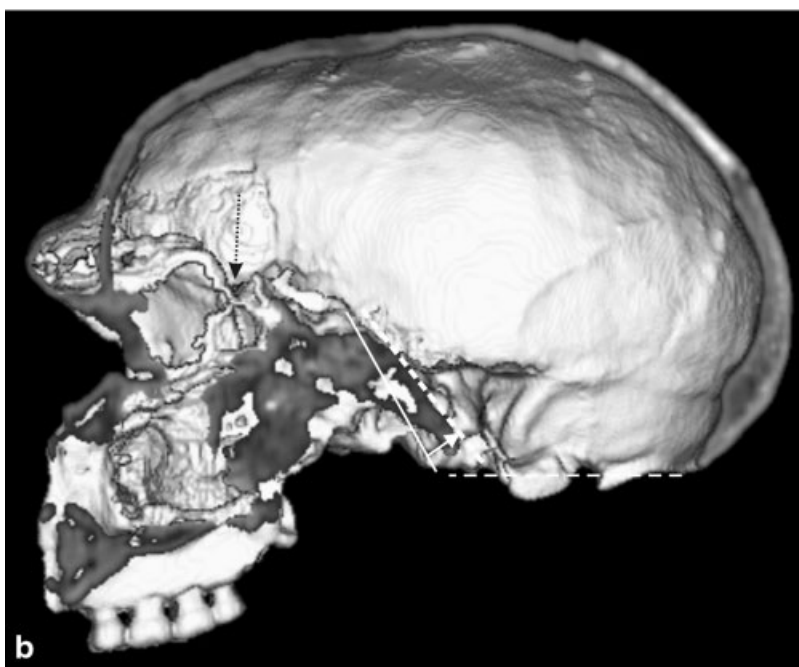


Figure 3. Deformations of the Steinheim cranium that cannot be detected externally. **a:** This endocranial view shows the lateral shift of the mid-sagittal plane and its rotation by two different angles: α_1 for *crista galli* and α_2 for the perpendicular plate of the ethmoid bone. The maxillae have been shifted toward the right by a distance δ_1 , and the molar region of the left dental arch has also been pushed upward by a distance δ_2 . The right orbital plate has been bent into a bubble by at least a distance Δ . The circle of dots highlights a foramen that had been almost completely filled with sediment (as is visible in Figure 2c); the erode/dilate operation has opened it satisfactorily. The black arrow with the dotted shaft points to the tip of the *crista galli*; the white arrow with the dotted shaft points to a lamella in the maxillary antrum. The sequence of five short black arrows points to where the encrustation and the fossilized bone have a common edge; it is barely visible, again manifesting how well the erode/dilate algorithmic sequence operates (see also Figure 5b). The sequence of five short white arrows indicates a crack in the fossilized bone, which has been segmented successfully; it is not visible in the encrusted specimen (see Figure 2c). **b:** A sagittal section of the cranium near the mid-sagittal plane shows how the clivus and the anterior rim near opisthion have been pushed anteriorly, thus decreasing the height of the cranium. The incline of the clivus is too low. The short white arrow indicates the estimated extent and direction of this deformation. The estimate of the deformation on its own explains why the endocranial volume found by counting voxels is smaller than the *in vivo* volume. The black arrow with the dotted shaft points to the *sella turcica*. **c:** A detail of the inner frontal vault, showing how the inner table has been pushed into the orbital plate (the orbital plate should be roughly horizontal). Consequently, the anterior fossa is too pointed; therefore, the computed endocranial volume underestimates the original ("undeformed") brain case volume (compare with Figure 5b).



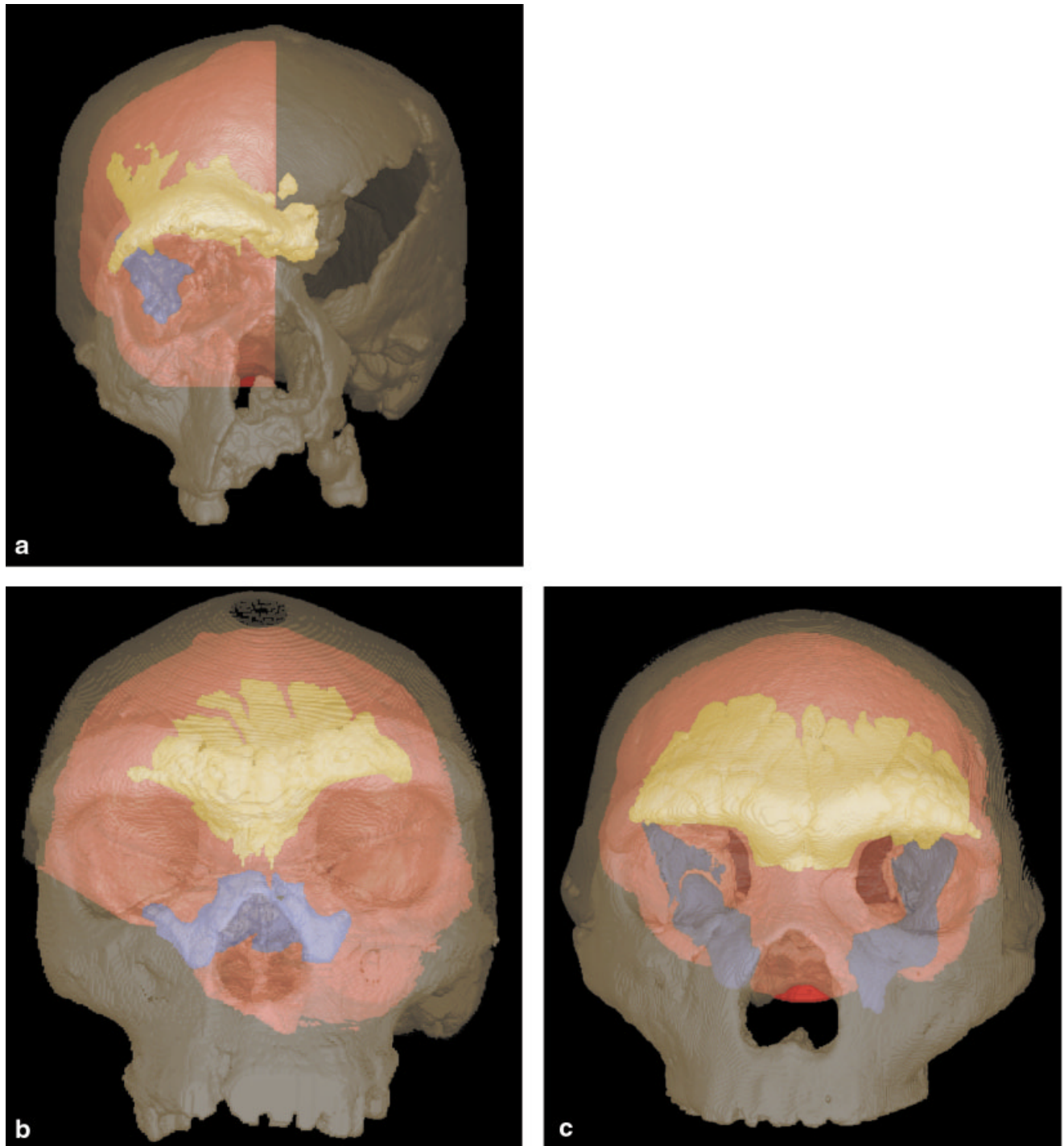


Figure 4. The paranasal sinuses of Steinheim (**a**), Petralona (**b**), and Broken Hill (Kabwe; **c**) in semitransparent views. Red: endocast of the braincase; blue: sphenoid sinus; yellow: frontal sinus. The frontal sinuses of the two European fossils extend laterally beyond the orbital rims. At their outermost extension, they are separated by the two very thin (~3 mm) compacta of the sphenoidal and frontal bones from the sphenoidal sinuses, which also extend far laterally. The African mid-Pleistocene cranium (Broken Hill, which is roughly contemporaneous) does not have such a laterally extended pneumatization—neither of the frontal, nor of the sphenoidal sinus.

below the cribriform plate and inside the maxillary antrum (Figure 2d), and part of the *sella turcica* (Figure 3b). The partial absence of the latter indicates that the cranium suffered losses before the encrustation process began.

The cranium is strongly deformed in several different directions: the maxillae away from midline toward the right, being twisted in the process (Figure 3a). The inner surface of the frontal bone behind the browridges

has been broken and the whole vault, therefore, is collapsed downward by approximately 1 cm (Figure 3c). The right orbital plate of the frontal bone, thus, is deformed and appears in cross-section like a bubble (Figure

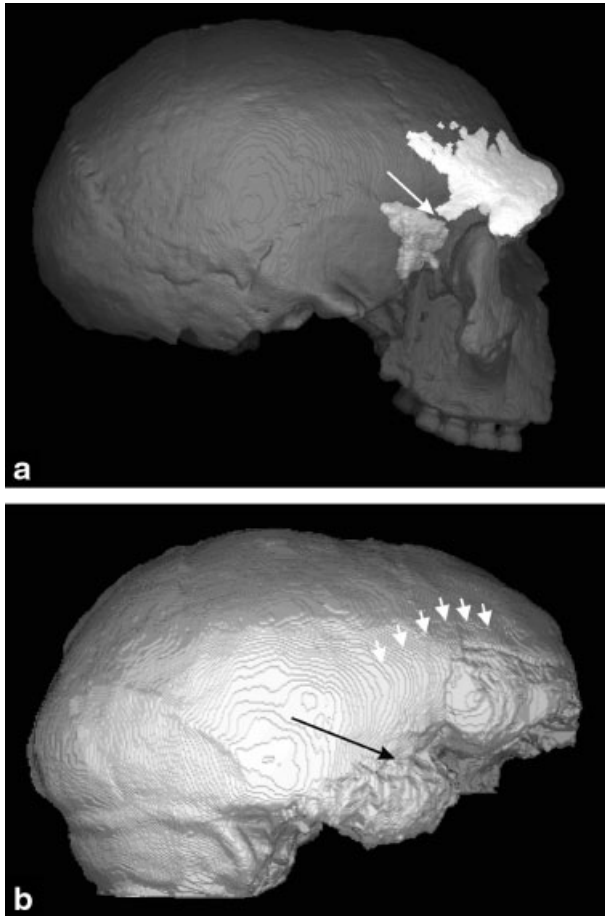


Figure 5. Features of the endocast of the Steinheim cranium. **a:** The relative position of the frontal sinus (white) and the sphenoidal sinus (gray) show their proximity. The bone (shown by an arrow) separating these two sinuses is approximately 3 mm thick. **b:** The virtual endocast of the right side of the Steinheim cranium. Contour steps are 0.5 mm apart; the volume of this endocast, found by counting voxels, is 445 cm³. The frontal lobe is pointed due to deformation of the cranial vault (compare Figure 3c). Electronic preparation clearly shows the lateral sulcus (sylvian sulcus, long black arrow). The sequence of six short white arrows shows the posterior surface edge where the encrustation in the original specimen and the fossilized bone meet. All voxels of the endocast anterior to this boundary have been found by removal of the encrustation(s). The slight ridge designated by these arrows shows that the erode/dilate algorithm cannot completely smooth away artifacts of the segmentation methodology, but it has done so quite successfully nonetheless (compare Figure 3a). The removal of the encrustations shows the morphology of the right anterior part of the frontal lobe as well as the imprint of a crack in the fossilized frontal bone (compare Figures 2d and 3a). We note that the erosion/dilation algorithms have preserved this crack, demonstrating their appropriateness for electronic segmentation methodology.

3a,b). Weinert (1936) had already noted several exocranial deformations and considered them in his description of the skull, but the internal deformations revealed here clarify and correct some of his conclusions (see below).

Externally, the vault shows a reasonably planar mid-sagittal plane (Weinert, 1936), but not internally. The *pars orbitalis* of the right frontal bone must, in a future reconstruction, be bent inferiorly, whereas the *crista galli* and the perpendicular plate of the ethmoid bone must be rotated by two different angles (Figure 3a) into the mid-sagittal plane, a process that will give the face a broad, large appearance, as already suggested by Wolpoff (1980) and at odds with Weinert's original appraisal.

Weinert, in his 1936 description, also pointed out, for example, that basion was too high (i.e., the overall cranial height, as determined by the basion–bregma distance was too small). From the CT scan, we can observe that the inclination of the clivus is re-

sponsible for this small height (Figure 3b). Weinert also noted the receding frontal; however, our presentation here shows that, originally, the frontal must have been steeper, comparable in its morphology with that of the mid-Pleistocene Petralona specimen (Kokkoros and Kanellis, 1960). Weinert notes the overall “gracile” appearance of the cranium. We disagree with this assessment: when the deformations are reversed, then the cranium will be quite broad and have a much more massive appearance. In the same vein of assessment, Weinert describes the face as not very wide; the internal deformations (Figure 3a) clearly show that Weinert's error is due to his inability to assess what deformations changed the morphology of the face, all of them making the present fossil's face appear smallish and narrow.

To describe the extent of the paranasal sinuses, which is little affected by these deformations, we use the developed image editing methods for their isolation (Prossinger et al.,

2000a): after having removed the encrustations, we electronically fill these sinuses and virtually dilate their surfaces before eroding. We then apply the same methods, suitably modified, to the sinuses of the mid-Pleistocene crania Petralona (Kokkoros and Kanellis, 1960) and Broken Hill/Kabwe (Woodward, 1921).

The frontal sinuses of Petralona and Steinheim are astonishingly similar: they both extend laterally beyond the supraorbital arch of the browridge (Figure 4a,b); the Broken Hill frontal sinus, on the other hand, does not (Figure 4c). The frontal sinuses of Broken Hill and Petralona are only somewhat larger at glabella than the Steinheim sinus; perhaps enlarged frontal sinuses enhance mechanical stability, especially if these have internal lamellae, as noted in Bookstein et al. (1999) and Prossinger et al. (2000b). In the context of the debate about the role of the frontal sinuses and the morphology of the browridge, the large extent of the frontal sinuses in Steinheim revealed in this study

will rekindle the debate about masti-catory stress vs. supraorbital torus formation hypotheses (Prossinger et al., 2000b; Ravosa et al., 2000).

The sphenoidal sinuses of Petralona and Steinheim are also remarkably similar in that both extend far into the temporal fossa of the frontal bone. In the case of the Steinheim cranium, the frontal and the sphenoidal sinuses are separated by a thin bone approximately 3 mm thick (Figure 5a). The morphology of the Broken Hill sphenoidal sinus is very different: the sphenoid wings are pneumatized only at the base of the cranium; these hollows do not extend much (laterally) beyond a parasagittal plane defined by the midpoints of the orbits. The sphenoidal sinuses of Steinheim and Petralona appear disjoint at the base due to the incompleteness of the skull base (eroded clivus) in the two European specimens.

Lieberman (2000) discusses brow-ridge growth, particularly in the context of growth field distributions which were first introduced by Enlow (1990). In his analysis, he compares the ontogeny of the browridges in various taxa. The absence of allometric relations for fossil hominins in that study is noteworthy. In the case of *H. sapiens*, he endorses the view that variations in browridge morphology are to be ascribed to differences in growth field distributions. As the frontal sinuses of Steinheim, Petralona, and Broken Hill/Kabwe presented in this study show, future investigations of this topic must take into consideration that all three specimens show similar growth field mechanisms in the mid-sagittal plane (as proposed by Enlow, 1990, and illustrated in Figure 6 of Lieberman, 2000), but in the case of archaic *Homo*, there is the added issue of a difference in the lateral extent of such growth fields, where a difference between the European and the African specimens must be taken into account.

Although we can compare only three specimens, we do note that the two fossil crania with dramatic lateral extensions of paranasal sinuses are attributed to *H. heidelbergensis* from Europe; the African one differs. This observation suggests that the *Homo* taxon in Europe may be different from an African one.

VOLUME ESTIMATIONS

The deformations along the inner table of the Steinheim braincase are considerable. Here, we mention those multidirectional endocranial deformations that relate to braincase volume (a surrogate for brain volume) estimations. Assessing the magnitude of these deformations and their influence on our volume estimate yields an uncertainty measure, which is indispensable for comparison with other mid-Pleistocene crania volumes (Weber et al., 1998; Prossinger et al., 2000a).

Because the left-hand side of the Steinheim cranium is broken and incomplete, we find the endocranial volume by first estimating a mid-sagittal plane. We use the remarkable near-coplanarity of glabella, bregma, lambda, and inion to define the mid-braincase plane. We filled the boundary between this plane and the inner table slice-wise, after plugging (with an image-edited boundary) foramina, fissures, and breaks. The right endocranial structure is complete enough to use anatomical features as guidance. The posterior part of the foramen magnum is extensively broken away, so we created a surface by interconnecting points on the rim. After smoothing, the resulting surface of the virtual endocast seemed satisfactory enough (Figure 4b) to find a lower boundary for the braincase volume. Volume estimation is straightforward: count the number of voxels in the endocranium and multiply by the volume of one voxel. Our algorithmically derived estimate for the lower limit is 990 cm³. Due to the uncertainties introduced by an incomplete braincase and the many deformations, we refrain from using refined techniques of half-height estimations to modify our result (Weber et al., 1998).

The deformations of the inner table of the frontal vault (Figure 3c) and the clivus being pushed upward by more than 1 cm at basion (Figure 3b) make this volume estimation by far the lowest possible. The *crista galli* and the *sella turcica*, being pushed laterally toward the left parietal (Figure 3a), further reduce the volume. Thus, any corrections for deformation can only increase the braincase volume. We

used the measured volume of the region between *crista galli* (as presently positioned in the deformed cranium) and the mid-sagittal plane (being approximately 30 cm³) as an uncertainty estimator. We conclude that the realistic braincase volume is underestimated by approximately 150 cm³. Our analysis indicates that the Steinheim braincase volume is 1,140 cm³ (with an estimated upper limit 1,200 cm³ and an estimated lower limit 1,110 cm³), a value considerably larger than Ruff's estimate of around 950 cm³ (Ruff et al., 1997). Of the many attempts at guessing the cranial volume, Weinert (1936) came closest to our determination, although many other workers have achieved results that are notably different; an exhaustive list is given in DeMiguel and Henneberg (2001). The volumes of Petralona and Broken Hill are 1,170 (± 30) cm³ and 1,270 (± 10) cm³, respectively (Seidler et al., 1997). We conclude that the Steinheim cranium must have originally been comparable in size to other *H. heidelbergensis* crania, a conclusion considerably different from published descriptions (Wolpoff, 1999).

CONCLUSIONS

We believe that the estimated surfaces in our electronically segmented Steinheim cranium are correct to the nearest 0.5 mm (or less, on average) in each coordinate direction. This precision will allow the three-dimensional position measurements of both endo- and exocranial landmarks on the Steinheim fossil, which we use for morphometric analyses (Bookstein et al., 1999).

The external appearance of the Steinheim cranium has led most researchers to diagnose it as female. The assessment of the extent of the internal deformations clearly show that such an attribution must be reconsidered: either the sexual dimorphism in mid-Pleistocene humans is less marked, or the Steinheim cranium is possibly male. Furthermore, its position in the debate of being a proto-Neanderthal (Wolpoff, 1980; Stringer, 1985) must be reviewed, because the evaluations of the external morphologies must be reconsidered in light of the discovered multidirected distor-

tions/deformations visible internally. In this study, we refrain from such a reconsideration, because we believe that any such undertaking is risky; only after a proper mathematical “undeformation” has reversed the distortions can morphologic descriptions of the form be considered trustworthy.

The possibility of algorithmic filtering and image editing are only two advantages of using CT scans of fossilized specimens. Electronic preparation techniques allow detailed assessments of “hidden” features and difficult-to-see deformations. Only af-

University of Vienna, for help with the data file handling. A. Juetter's (Konrad Lorenz Institute for Evolution and Cognition Research, Altenberg) assistance with the color graphics is gratefully appreciated.

LITERATURE CITED

The possibility of algorithmic filtering and image editing are only two advantages of using CT scans of fossilized specimens. Electronic preparation techniques allow detailed assessments of “hidden” features and difficult-to-see deformations.

ter “cleaning” can mathematical “undeformation” be undertaken. These applications to CT scans, and some presented insights found herewith, augment other methodologies used to unravel morphological (perhaps also evolutionary) relationships in the human fossil record.

ACKNOWLEDGMENTS

We thank M. Wolpoff, Department of Anthropology, University of Michigan, for discussions and suggestions and G. Weber, Inst. f. Anthropology,

- Adam KD. 1985. The chronological and systematic position of the Steinheim skull. In: Delson E, editor. *Ancestors: The hard evidence*. New York: Alan Liss. p 272–276.
- Berckheimer F. 1933. Ein Menschen-Schädel aus den diluvialen Schottern von Steinheim a.d. Murr. *Anthrop Anz* X:318.
- Bookstein F, Schäfer K, Prossinger H, Seidler H, Fieder M, Stringer C, Weber GW, Arsuaga J-L, Slice D, Rohlf FJ, Recheis W, Mariam A, Marcus L. 1999. Comparing frontal cranial profiles in archaic and modern *Homo* by morphometric analysis. *Anat Rec (New Anat)* 257:217–224.
- DeMiguel C, Henneberg M. 2001. Variation in hominoid brain size: How much is due to method? *Homo* 52:3–58.
- Enlow DH. 1990. *Facial growth*. 2nd ed. Philadelphia: WB Saunders.
- Hounsfield GN. 1973. Computerized transverse axial scanning (tomography): Part I. Description of the system. *Br J Radiol* 46:1016–1022.
- Kokkoros P, Kanellis A. 1960. Découverte d'un crane d'homme paléolithique dans péninsule Chalcidique. *Anthropologie* 64: 132–147.
- Lieberman DE. 2000. Ontogeny, homology, and phylogeny in the hominid craniofacial skeleton: The problem of the browridge. In: O'Higgins P, Cohn M, editors. *Development, growth and evolution: Implications for the study of the hominid skeleton*. Linnean Society Symposium Series No. 20. San Diego: Academic Press. p 85–122.
- Prossinger H. 1999. Electronic preparation of fossilized skulls, notably Steinheim. In: Šabik D, Vigner J, Vigner M, editors. *IVth International Anthropological Congress of Aleš Hrdlička*, Prague. p 125.
- Prossinger H, Weber GW, Seidler H, Recheis W, Ziegler R, zur Nedden D. 1998. Electronically aided preparation of fossilized skulls: Medical imaging techniques and algorithms as an innovative tool in paleoanthropological research. *Am J Phys Anthropol* 26(Suppl):181.
- Prossinger H, Wicke L, Seidler H, Weber GW, Recheis W, Müller G. 2000a. The CT scans of fossilized crania with encrustations removed allow morphological and metric comparisons of paranasal sinuses. *Am J Phys Anthropol* 30(Suppl):254.
- Prossinger H, Bookstein F, Schäfer K, Seidler H. 2000b. Reemerging stress: Supraorbital torus morphology in the midsagittal plane? *Anat Rec (New Anat)* 261: 170–172.
- Ravosa JM, Vinyard CJ, Hylander WL. 2000. Stressed out: Masticatory forces and primate circumorbital form. *Anat Rec (New Anat)* 261:173–175.
- Ruff CB, Trinkaus E, Holliday TW. 1997. Body mass and encephalization in Pleistocene *Homo*. *Nature* 387:173–176.
- Seidler H, Falk D, Stringer C, Wilfing H, Müller G, zur Nedden D, Weber GW, Recheis W, Arsuaga J-L. 1997. A comparative study of stereolithographically modeled skulls of Petralona and Broken Hill: Implications for future studies of middle Pleistocene hominid evolution. *J Hum Evol* 33:691–703.
- Spoor CF, Zonnefeld FW, Macho GA. 1993. Linear measurements of cortical bone and dental enamel by computed tomography: Applications and problems. *Am J Phys Anthropol* 91:469–484.
- Spoor F, Jeffrey N, Zonnefeld F. 2000. Imaging skeletal growth and evolution. In: O'Higgins P, Cohn M, editors. *Development, growth and evolution: Implications for the study of the hominid skeleton*. Linnean Society Symposium Series No. 20. San Diego: Academic Press. p 123–161.
- Stringer CB. 1985. Middle Pleistocene hominid variability and the origin of late Pleistocene humans. In: Delson E, editor. *Ancestors: The hard evidence*. New York: Alan Liss. p 272–276.
- Weber GW, Recheis W, Scholze T, Seidler H. 1998. Virtual anthropology (VA): Methodological aspects of linear and volume measurements—first results. *Coll Antropol* 22:575–583.
- Weinert H. 1936. Der Urmenschenschädel von Steinheim. *Z Morphol Anthropol* XXXV:463–517.
- Wolpoff MH. 1980. Cranial remains of middle Pleistocene European hominids. *J Hum Evol* 9:339–358.
- Wolpoff MH. 1999. *Paleoanthropology*. 2nd ed. Boston: McGraw Hill. p 527.
- Woodward AS. 1921. A new cave man from Rhodesia. *Nature* 108:371–372.